


# Chaotic bursting and burst synchronization in a discrete dual-Rulkov neural network with memristive synaptic coupling

Ke Meng(孟珂), Yifan Bu(卜一帆), Yinghong Cao(曹颖鸿), Suo Gao(高锁), Qi Li(李琦), Chunpeng Wang(王春鹏), and Jun Mou(牟俊)

**Citation:**Chin. Phys. B, 2026, 35 (**6**): 060501. DOI: 10.1088/1674-1056/ae5f06
http://cpb.iphy.ac.cn; http://iopscience.iop.org/cpb

**What follows is a list of articles you may be interested in**

---

## Spiking-bursting alternating chaos mediated by a locally active memristor

Yuxia Li(李玉霞), Xintong Yue(岳新同), Hui Chang(常辉), Baoxing Han(韩宝兴), and Yan Zhang(张燕)
Chin. Phys. B, 2026, 35 (**3**): 030504. DOI: 10.1088/1674-1056/ae44f9

## Dynamics analysis and DSP implementation of the Rulkov neuron model with memristive synaptic crosstalk

Yichen Bi(毕毅晨), Jun Mou(牟俊), Herbert Ho-Ching Iu, Nanrun Zhou(周南润), Santo Banerjee, and Suo Gao(高锁)
Chin. Phys. B, 2026, 35 (**1**): 010504. DOI: 10.1088/1674-1056/ae1728

## Energy adaptive regulation of a multifunctional neuron circuit

Xi-Kui Hu(胡锡奎), Juan Yang(杨娟), and Ping Zhou(周平)
Chin. Phys. B, 2026, 35 (**1**): 010503. DOI: 10.1088/1674-1056/ae1451

## Design of a memristive chaotic map and its adaptive regulation

Ya Wang(王亚), Xin-Lin Song(宋欣林), and Fei-Fei Yang(杨飞飞)
Chin. Phys. B, 2025, 34 (**9**): 090504. DOI: 10.1088/1674-1056/adea5c

## A novel non-autonomous hyperchaotic map based on discrete memristor parallel connection

Weiping Wu(吴伟平), Mengjiao Wang(王梦蛟), and Qigui Yang(杨启贵)
Chin. Phys. B, 2025, 34 (**5**): 050503. DOI: 10.1088/1674-1056/adb8bc

---

**SPECIAL TOPIC — Biophysical circuits: Modeling & applications in neuroscience**

# Chaotic bursting and burst synchronization in a discrete dual-Rulkov neural network with memristive synaptic coupling

Ke Meng(孟珂)[1], Yifan Bu(卜一帆)[2], Yinghong Cao(曹颖鸿)[1,†], Suo Gao(高锁)[1], Qi Li(李琦)[3,4], Chunpeng Wang(王春鹏)[3,4], and Jun Mou(牟俊)[1]

[1] *School of Information Science and Engineering, Dalian Polytechnic University, Dalian* 116034, *China*
[2] *Zhongshan School of Medicine, Sun Yat-sen University, Guangzhou, Guangdong* 510080, *China*
[3] *Key Laboratory of Computing Power Network and Information Security, Ministry of Education, National Supercomputer Center in Jinan, Qilu University of Technology (Shandong Academy of Sciences), Jinan* 250353, *China*
[4] *Shandong Provincial Key Laboratory of Computer Networks, Shandong Fundamental Research Center for Computer Science, Jinan* 250013, *China*

(Received 14 March 2026; revised manuscript received 7 April 2026; accepted manuscript online 14 April 2026)

A discrete dual-Rulkov neural network with memristive synaptic coupling is constructed to investigate chaotic bursting dynamics and burst synchronization. First, a memristive synapse model suitable for discrete-time neurons is established, and its pinched hysteresis loop (PHL) fingerprint and local activity are verified. Based on this synapse model, a five-dimensional memristively coupled discrete neural system is formulated. By combining Lyapunov exponent spectra (LEs), bifurcation analysis, and equilibrium stability analysis, chaotic and hyperchaotic bursting behaviors induced by variations in the coupling gain are revealed, together with their dynamical evolution characteristics. Furthermore, to characterize irregular spiking activities during chaotic bursting, a joint framework based on the phase-locking value (PLV) and burst envelope correlation (EnvCorr) is introduced, through which three bursting regimes, namely, in-phase bursting (IPB), phase-shifted bursting (PSB), and desynchronized bursting (DB), are identified. Finally, a digital signal processor (DSP)-based real-time hardware implementation is carried out, and the good qualitative agreement between experimental and numerical results demonstrates the physical feasibility of the proposed model.

**Keywords:** memristor, Rulkov neuron, chaotic bursting, burst synchronization, DSP implementation

**PACS:** 05.45.–a, 05.45.Xt, 87.19.lj, 87.19.lg

**DOI:** 10.1088/1674-1056/ae5f06 **CSTR:** 32038.14.CPB.ae5f06

## 1. Introduction

Neuronal synchronization and rhythmic oscillations are widely regarded as important intermediate-level phenomena linking single-neuron firing activities to brain functions.[1–4] Buzséki and Draguhn[5] pointed out that cortical networks can generate behavior-related oscillations across multiple frequency bands and that these oscillations are not merely by-products but are closely associated with sensory integration, motor control, and cognitive processing. Meanwhile, burst firing, as an important neuronal dynamic pattern distinct from single-spike firing, is also considered to play a special role in neural coding and information transmission.[6–9] Krahe and Gabbiani[10] pointed out in their review of sensory systems that bursts often represent a signaling mode different from isolated spikes and can convey more salient stimulus information. At the network level, Yu *et al.*[11] investigated chaotic phase synchronization in small-world networks of bursting neurons and found that synchronization can first emerge at the bursting time scale, whereas asynchronous behavior may still persist at the spiking time scale. Batista *et al.*[12] analyzed phase synchronization in bursting neuronal networks with clustered small-world topology and obtained the corresponding critical coupling conditions. These studies indicate that neuronal synchronization and bursting activity are of great significance in brain information processing and further suggest that the synchronization patterns of complex bursting behaviors still need to be characterized in a more refined manner. Recent studies have further expanded this line of research from conventional neuronal synchronization to more complex synchronization scenarios in memristive and neuromorphic systems, including synchronization in memristor-coupled discrete heterogeneous neuron networks,[13] bursting synchronization in $VO_2$-memristor/Josephson-junction neuromorphic systems,[14] and phase-locking value (PLV)-based synchronization characterization in large-scale heterogeneous neural networks.[15] These developments further highlight the necessity of introducing refined quantitative measures for complex burst synchronization. In addition, recent studies have also extended synchronization analysis to physical-neuron and neural-circuit-related systems, where synchronization behavior has been investigated together with energy evolution and control, further enriching the understanding of coordinated

[†]Corresponding author. E-mail: caoyinghong@dlpu.edu.cn

© 2026 Chinese Physical Society and IOP Publishing Ltd. All rights, including for text and data mining, AI training, and similar technologies, are reserved.

neural dynamics.[16,17]

In recent years, memristors have attracted extensive attention in the field of neuromorphic computing because of their nonlinearity, history dependence, and tunable conductance.[18–22] Chua[23] proposed the memristor in 1971 as the "fourth fundamental circuit element" from the perspective of circuit theory. Later, Strukov *et al.*[24] reported a representative physical realization in 2008, which promoted the development of memristive systems from theoretical concepts to device implementation and practical applications. On this basis, Zidan *et al.*[25] pointed out that electronic devices based on memristive systems possess significant potential in on-chip storage, brain-inspired computing, and in-memory computing. For neuromorphic applications, Huang *et al.*[26] reviewed various memristive artificial synapses and showed that such devices can emulate multiple synaptic functions under electrical or optical stimuli, thus serving as key building blocks for efficient neuromorphic systems. Kuzum *et al.*[27] also systematically summarized the materials, devices, and applications of synaptic electronics, and emphasized the advantages of memristive devices in mimicking synaptic plasticity and enabling brain-inspired computing. Therefore, the introduction of memristors as artificial synapses with memory into neuronal network modeling is not only physically well motivated, but also provides a new coupling mechanism for the study of complex neural dynamics.[28] Meanwhile, recent advances in memristive neuromorphic circuits have further demonstrated the versatility of memristors in associative memory,[29] multisensory information processing,[30,31] adaptive attention,[32] and bioinspired decision-making,[33] which further strengthens their physical relevance as artificial synapses and functional circuit elements in brain-inspired systems.

With respect to neuronal modeling, how to balance biological plausibility, dynamical richness, and computational efficiency remains a central issue in neural dynamics.[34–38] Izhikevich pointed out in his comparison of spiking neuron models that model selection should balance biological realism against the computational cost of large-scale simulations.[39] In this context, the two-dimensional discrete map proposed by Rulkov,[40] which contains one fast variable and one slow variable, can effectively reproduce the spiking and spiking-bursting behaviors commonly observed in experiments, and can also be used to investigate synchronization phenomena between coupled neurons. Furthermore, Ramírez-Ávila *et al.*[41] conducted a detailed investigation of the dynamical responses of the Rulkov neuron model and pointed out that the two-dimensional Rulkov map, as a computationally inexpensive discrete model, can effectively reproduce the spiking and bursting behaviors of real biological neurons, thereby making it suitable for large-scale network dynamical analysis. In addition, Wagemakers and Sanjuán[42] implemented the chaotic Rulkov neuron model using an electronic circuit and showed that this type of map-based neuron model possesses good hardware realizability. Therefore, the discrete Rulkov neuron model provides an appropriate platform for investigating chaotic bursting dynamics and burst synchronization under memristive synaptic coupling, owing to its strong dynamical expressiveness and advantages in digital implementation. In parallel, discrete memristive neuron-like arrays and Josephson-junction-based networks have exhibited increasingly rich dynamical behaviors, including disordered spiral waves, controllable spatiotemporal patterns, bursting synchronization, and alternating spiking–bursting chaos.[43–45] Related studies on discrete memristive synapse networks, multistable discrete neuron maps, memristor-coupled chaotic circuits, and hardware-oriented implementations further indicate that discrete-time memristive neural modeling has become an active and rapidly developing research direction.[46–50] More broadly, this trend has also been accompanied by engineering-oriented extensions involving chaotic-map design, symmetry construction, image-encryption-related applications, map reconstruction, and attractor control.[51–54]

Although substantial progress has been made in the study of firing patterns, chaotic dynamics, and synchronization behaviors in memristively coupled neuronal systems, a dedicated characterization of complex burst synchronization patterns during chaotic bursting is still lacking. In particular, when spiking activities become highly irregular, conventional synchronization measures are often insufficient to distinguish different coordinated bursting regimes. Moreover, within this context, the parameter-dependent dynamical evolution associated with these burst synchronization patterns has not yet been clarified in a sufficiently systematic manner, and real-time digital hardware validation of such behaviors remains relatively limited. Motivated by these issues, this paper focuses on the complex bursting dynamics and burst synchronization patterns in a discrete dual-Rulkov neural system coupled through a memristive synapse.

To address the above issues, a pair of Rulkov neurons coupled through a discrete memristive synapse is constructed in this paper, and the complex bursting dynamics together with the burst synchronization patterns under varying coupling gain are systematically investigated. First, a memristive synapse model suitable for the iterative framework of discrete neurons is established, and its pinched hysteresis loop (PHL) fingerprint and local activity are verified. Then, a five-dimensional memristively coupled discrete neural system is formulated. By combining Lyapunov exponent spectra (LEs), bifurcation analysis, and equilibrium stability analysis, the chaotic and hyperchaotic bursting behaviors of the system, as well as their parameter-dependent dynamical evolution, are revealed. Furthermore, to characterize irregular spiking activities during

chaotic bursting, a joint analysis framework based on phase-locking value (PLV) and burst envelope correlation (EnvCorr) is introduced, through which three bursting regimes, namely in-phase bursting (IPB), phase-shifted bursting (PSB), and desynchronized bursting (DB), are identified. Finally, real-time hardware implementation is carried out on a digital signal processor (DSP) platform, and the good qualitative agreement between the experimental results and numerical simulations demonstrates the physical feasibility of the proposed model.

The main contributions of this paper can be summarized as follows:

(i) A memristive synapse model suitable for discrete neuronal coupling is established, and its typical memristive fingerprint characteristics and local activity are verified.

(ii) A five-dimensional memristively coupled discrete system composed of two Rulkov neurons is formulated, and the chaotic/hyperchaotic bursting dynamics induced by the coupling gain are revealed.

(iii) For chaotic bursting signals with irregular spiking activities, a joint characterization framework based on PLV and EnvCorr is proposed to distinguish three bursting regimes: IPB, PSB, and DB.

(iv) DSP-based real-time hardware experiments were conducted to verify the physical feasibility of the proposed model and the qualitative consistency between the numerical and experimental results.

## 2. Memristive synapse model and fundamental properties

This section introduces the discrete-time memristive synapse used for neuron coupling. The mathematical model is first presented, followed by the verification of its fingerprint characteristics and locally active property.

### 2.1. Mathematical model of the memristive synapse and discretization

A voltage-driven memristive synapse is considered to describe the history-dependent coupling between two neurons in discrete time. The synaptic driving signal is defined as the potential difference between the presynaptic and postsynaptic neurons:

$$v_s(t) = x_{\mathrm{pre}}(t) - x_{\mathrm{post}}(t), \tag{1}$$

where $x_{\mathrm{pre}}(t)$ and $x_{\mathrm{post}}(t)$ denote the membrane-potential-related state variables of the presynaptic and postsynaptic neurons, respectively.

An internal state variable $w(t)$ is introduced to represent the synaptic memory state. Its dynamics are described by a first-order system with leakage and external forcing

$$\dot{w}(t) = -\gamma w(t) + \eta v_s(t), \tag{2}$$

where $\gamma > 0$ is the decay coefficient and $\eta$ is the driving intensity. The memductance is defined as a bounded nonlinear function of the internal state

$$G(w) = g_0 + g_1 \tanh(w) - g_3 \tanh^3(w), \tag{3}$$

with $g_0$, $g_1$, and $g_3$ being constant parameters. The synaptic current is then expressed as

$$i_s(t) = kG(w(t))v_s(t), \tag{4}$$

where $k$ is the coupling gain. To match discrete-time neuron maps and facilitate iterative digital implementation, the forward Euler scheme with step size $h$ is applied to Eq. (2). The discrete-time state update equation is obtained as

$$w_{n+1} = w_n + h(-\gamma w_n + \eta v_{s,n}), \tag{5}$$

where

$$v_{s,n} = x_{\mathrm{pre},n} - x_{\mathrm{post},n}. \tag{6}$$

Accordingly, the discrete memductance and synaptic current are given by

$$G_n = g_0 + g_1 \tanh(w_n) - g_3 \tanh^3(w_n), \tag{7}$$

$$i_{s,n} = kG_n v_{s,n}. \tag{8}$$

Therefore, the discrete memristive synapse is described by the iterative map defined by Eqs. (5)–(8).

### 2.2. Fingerprint characteristics

The fingerprint characteristic of a memristive element is verified through the pinched hysteresis loop (PHL) in the $v$–$i$ plane under sinusoidal excitation. The discrete memristive synapse described by Eqs. (5)–(8) is driven by the AC voltage

$$v_s(t) = V_{\mathrm{m}} \sin(2\pi f t), \tag{9}$$

where $V_{\mathrm{m}}$ and $f$ denote the amplitude and frequency of the excitation signal, respectively.

Figure 1(a) illustrates the PHLs obtained for different excitation frequencies with a fixed amplitude $V_{\mathrm{m}}$. It is observed that all loops pass through the origin, confirming the pinched property. Moreover, as the frequency increases, the hysteresis loop becomes progressively thinner and its enclosed area decreases, indicating that the memory effect is weakened at higher frequencies and that the element tends toward an almost linear resistive behavior.

Figure 1(b) presents the PHLs under different excitation amplitudes with a fixed frequency $f$. The pinched property at the origin is also maintained. In addition, the hysteresis loop expands with increasing $V_{\mathrm{m}}$, implying stronger state-dependent modulation and an enhanced memory effect under larger excitation amplitudes.

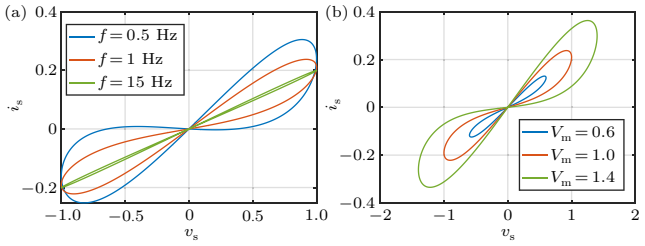



**Fig. 1.** PHLs of the discrete memristive synapse in the $v$–$i$ plane under sinusoidal excitation: (a) PHLs at different frequencies $f$ with fixed amplitude $V_m$; (b) PHLs at different amplitudes $V_m$ with fixed frequency $f$.

The above results demonstrate that the proposed discrete memristive synapse exhibits the typical fingerprint features of memristive systems, including the pinched hysteresis loop and its dependence on both excitation frequency and excitation amplitude. Unless otherwise specified, the parameters are set as $g_0 = 0.2$, $g_1 = 0.8$, $g_3 = 0.6$, $\gamma = 0.5$, $\eta = 1.0$, and $h = 0.003$.

### 2.3. Locally active property

The locally active property of the discrete memristive synapse is investigated through its DC $I$–$V$ characteristics. A quasi-static DC voltage $V$ is applied, i.e., $v_s(n) = V$, where $V$ is swept over a prescribed range. For each voltage value, the internal state $w$ is iterated according to Eq. (5) until convergence, and the corresponding steady-state current is recorded. Specifically, the DC current $I(V)$ is obtained by averaging the synaptic current over the last $M_a$ iterations after discarding the transient response:

$$I(V) = \frac{1}{M_a} \sum_{n=M_t+1}^{M_t+M_a} i_{s,n}, \tag{10}$$

where $M_t$ and $M_a$ denote the numbers of discarded transient steps and averaging steps, respectively, and $i_{s,n}$ is computed from Eq. (8).

Based on the DC response $I(V)$, the incremental conductance is defined as

$$g_{inc}(V) = \frac{dI(V)}{dV}, \tag{11}$$

which is evaluated numerically using finite differences. A locally active region is identified when $g_{inc}(V) < 0$, corresponding to negative differential resistance (NDR) behavior, whereas the synapse is locally passive when $g_{inc}(V) > 0$.

Figure 2(a) shows the obtained DC $I$–$V$ curve, and Fig. 2(b) presents the corresponding incremental conductance $g_{inc}(V)$. It is observed that $g_{inc}(V)$ becomes negative within a certain voltage interval, verifying the existence of a locally active region. The locally active and locally passive regions are marked by different colors in Fig. 2. The parameters are the same as those used in Subsection 2.2.

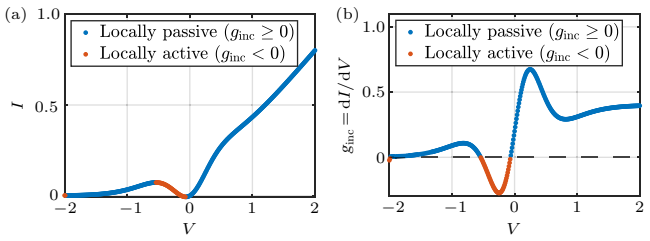



**Fig. 2.** DC characteristics of the proposed discrete memristive synapse: (a) DC $I$–$V$ curve; (b) incremental conductance $g_{inc}(V)$. The locally active ($g_{inc} < 0$) and locally passive ($g_{inc} > 0$) regions are highlighted in different colors.

## 3. Discrete dual-Rulkov neural system with memristive synaptic coupling

A memristively coupled discrete neuron network is formulated in this section by integrating the Rulkov map with the discrete memristive synapse introduced in Section 2. Two identical neurons are coupled through a memristive synapse to construct a low-dimensional system with rich nonlinear dynamics. The two neurons share the same intrinsic parameters $\alpha$, $\mu$, and $\sigma$.

### 3.1. Rulkov map neuron

The single-neuron dynamics are described by the Rulkov map

$$x_{n+1} = \frac{\alpha}{1+x_n^2} + y_n + I + u_n, \tag{12}$$

$$y_{n+1} = y_n - \mu(x_n - \sigma), \tag{13}$$

where $x_n$ denotes the fast membrane-potential-related variable, $y_n$ is the slow recovery variable, $I$ is the external bias, and $u_n$ represents the coupling input.

### 3.2. Memristive coupling and five-dimensional system

The two neurons are coupled via a discrete memristive synapse. Figure 3 depicts the overall topology of the proposed memristive-coupled neural network. The synaptic voltage difference is defined as

$$v_{s,n} = x_{1,n} - x_{2,n}. \tag{14}$$

The internal state of the memristive synapse evolves as

$$w_{n+1} = w_n + h(-\gamma w_n + \eta v_{s,n}), \tag{15}$$

and the memductance is given by

$$G_n = g_0 + g_1 \tanh(w_n) - g_3 \tanh^3(w_n). \tag{16}$$

Accordingly, the synaptic current is expressed as

$$i_{s,n} = kG_n v_{s,n}. \tag{17}$$

By injecting $+i_{s,n}$ and $-i_{s,n}$ into the fast variables of the two neurons, respectively, the memristive-coupled discrete neuron

network is written as the following five-dimensional map:

$$\begin{cases} x_{1,n+1} = \dfrac{\alpha}{1+x_{1,n}^2} + y_{1,n} + I + i_{s,n}, \\ y_{1,n+1} = y_{1,n} - \mu(x_{1,n} - \sigma), \\ x_{2,n+1} = \dfrac{\alpha}{1+x_{2,n}^2} + y_{2,n} + I - i_{s,n}, \\ y_{2,n+1} = y_{2,n} - \mu(x_{2,n} - \sigma), \\ w_{n+1} = w_n + h[-\gamma w_n + \eta(x_{1,n} - x_{2,n})]. \end{cases} \tag{18}$$

Eqs. (18) constitute a five-dimensional discrete-time dynamical map with the state vector

$$\boldsymbol{X}_n = (x_{1,n}, y_{1,n}, x_{2,n}, y_{2,n}, w_n)^{\mathrm{T}}.$$

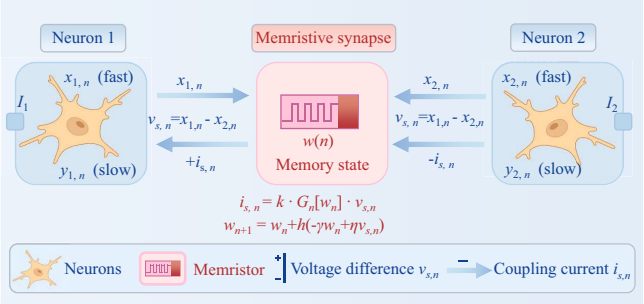



**Fig. 3.** Schematic diagram of the memristively coupled Rulkov neuron network, where two identical Rulkov neurons are connected through a discrete memristive synapse. The synaptic voltage difference drives the memristive state $w_n$, and the resulting synaptic current $i_{s,n}$ is injected into the two neurons with opposite signs.

## 4. Dynamical characterization of chaotic bursting and burst synchronization

In this section, the chaotic bursting dynamics and burst synchronization behaviors of the proposed memristively coupled dual-Rulkov system are investigated. First, burst synchronization is quantified by combining PLV and burst EnvCorr. Then, the global dynamical evolution of the system is analyzed through LEs and bifurcation diagrams, and the corresponding local stability characteristics are further interpreted via equilibrium analysis. All the dynamical phenomena discussed below are examined under two representative parameter sets, denoted as Set A and Set B, whose specific values are listed in Table 1. Finally, the burst synchronization regimes induced by the coupling gain are identified and discussed.

The two parameter sets are selected with reference to the classical bursting parameter regions of the Rulkov map reported in the literature and are further refined through preliminary numerical exploration of the present memristively coupled system.[41] Specifically, two representative sets that can stably generate distinct burst morphologies are retained for detailed analysis: Set A corresponds to rectangular bursting, whereas Set B corresponds to triangular bursting. Therefore, the two sets are adopted here not as isolated numerical examples, but as representative cases for examining the proposed synchronization analysis framework under different bursting waveforms. The memristive synapse parameters are kept unchanged, while the intrinsic parameters of the Rulkov map are adjusted.

**Table 1.** Two representative parameter sets and initial conditions for rectangular and triangular bursting, with $k \in (-1,1)$, $N = 2\times10^5$, and $N_0 = 5\times10^4$.

| Parameter type | Rectangular bursting | Triangular bursting |
|---|---|---|
| Rulkov parameters | $\alpha = 4.1$, $\mu = 0.001$, $\sigma = -1.2$, $I = 0$ | $\alpha = 3.85$, $\mu = 0.003$, $\sigma = -1.4$, $I = 0$ |
| Memristive-synapse parameters | $g_0 = 0.2$, $g_1 = 0.8$, $g_3 = 0.6$, $\gamma = 0.5$, $\eta = 1.0$, $h = 0.003$ | $g_0 = 0.2$, $g_1 = 0.8$, $g_3 = 0.6$, $\gamma = 0.5$, $\eta = 1.0$, $h = 0.003$ |
| Coupling gain | $k \in (-1,1)$ | $k \in (-1,1)$ |
| Initial conditions | $(-1.0,-2.0,-1.1,-2.1,0.1)$ | $(-1.0,-2.0,-1.1,-2.1,0.2)$ |

### 4.1. Quantification of burst synchronization

Burst synchronization in this work is characterized at the burst scale rather than by exact spike-by-spike alignment. This treatment is adopted because the memristively coupled dual-Rulkov system exhibits chaotic bursting with highly irregular intraburst spiking activities, for which direct pointwise waveform matching is no longer suitable for evaluating coordinated behaviors between the two neurons. Instead, synchronization is quantified from two complementary aspects, namely, the stability of the phase relation and the coherence of the slow burst envelopes.

Let $x_i(n)$ denote the post-transient samples of the fast variable, where $i = 1,2$. Since the raw bursting waveform contains sharp spike-like components that may distort Hilbert-phase estimation, a smoothed signal is first constructed by mean removal and moving-average filtering:

$$\tilde{x}_{i,n} = \frac{1}{W}\sum_{m=0}^{W-1}(x_{i,n-m} - \bar{x}_i), \quad i = 1,2, \tag{19}$$

where $\bar{x}_i$ denotes the sample mean of the retained data and $W$ is the window length. Based on the processed signals, burst synchronization behaviors are quantified below by the PLV and burst EnvCorr.

For reproducibility, the burst synchronization measures are computed through the following procedure: mean removal and moving-average smoothing of the post-transient fast signals, Hilbert-transform-based construction of analytic signals, extraction of instantaneous phase and burst envelope, PLV calculation from wrapped phase differences, and EnvCorr evaluation from the two burst envelopes.

#### 4.1.1. Phase-locking value

To quantify the stability of the phase relation between the two bursting signals, the analytic signal is obtained from $\tilde{x}_{i,n}$ through the Hilbert transform:

$$z_i(n) = \tilde{x}_{i,n} + j\,\mathcal{H}[\tilde{x}_{i,n}], \quad \phi_i(n) = \arg\big(z_i(n)\big), \tag{20}$$

where $\mathcal{H}[\cdot]$ denotes the Hilbert operator and $\phi_i(n)$ is the instantaneous phase of the $i$-th signal. The wrapped phase difference between the two neurons is then defined as:

$$\Delta\phi_n = \mathrm{wrapToPi}\big(\phi_1(n) - \phi_2(n)\big). \tag{21}$$

Based on $\Delta\phi_n$, the PLV is calculated by:

$$\mathrm{PLV} = \left| \frac{1}{M} \sum_{n=1}^{M} \mathrm{e}^{\mathrm{j}\Delta\phi_n} \right|. \tag{22}$$

The PLV measures the degree of concentration of the phase difference over time. When PLV $\to 1$, $\Delta\phi_n$ remains tightly distributed around a preferred phase lag, indicating a stable phase-locked relation. In contrast, when PLV $\to 0$, the phase difference is broadly distributed or continuously drifting, corresponding to weak or absent phase locking. In addition to the PLV itself, the probability density function (PDF) of $\Delta\phi_n$ is also examined to visualize the preferred phase-lag distribution.

It should be emphasized that the PLV reflects the stability of the phase relation rather than strictly implying IPB. Therefore, a large PLV may be obtained not only when the phase difference is concentrated around zero, but also when it is concentrated around a nonzero lag such as $\pi$. For this reason, the PLV alone is insufficient to fully distinguish different burst synchronization regimes, and it is further complemented by the burst EnvCorr introduced below.

In practice, the PLV is obtained by first removing the mean of each post-transient fast signal, then applying moving-average smoothing, constructing analytic signals via the Hilbert transform, extracting instantaneous phases, and finally averaging the complex phase-difference vectors according to Eq. (22).

#### 4.1.2. Burst envelope correlation (EnvCorr)

To quantify the coherence of bursting activity at the slow envelope scale, the envelope of each processed signal is extracted from the corresponding analytic signal as

$$\mathrm{env}_i(n) = |z_i(n)|, \quad i = 1,2. \tag{23}$$

Based on the extracted envelopes, the burst envelope correlation coefficient is defined as

$$\mathrm{EnvCorr} = \mathrm{corr}\big(\mathrm{env}_1(n), \mathrm{env}_2(n)\big). \tag{24}$$

The EnvCorr measures the similarity of the slow envelope evolution between the two neurons. When EnvCorr $\to 1$, the burst envelopes co-vary strongly in time, indicating highly coherent burst evolution. When EnvCorr $\to 0$, the EnvCorr is weak, implying poor coherence at the burst scale. Negative EnvCorr values indicate that the two envelopes tend to vary in an alternating or anticorrelated manner.

Compared with the PLV, which quantifies the stability of the phase relation, EnvCorr focuses on the similarity of the slow burst-envelope evolution. Therefore, EnvCorr provides complementary information for distinguishing different burst synchronization regimes. In particular, a large PLV may still appear when the phase difference is stably concentrated around a nonzero lag, whereas the corresponding burst envelopes may be only weakly correlated or even anticorrelated. For this reason, the joint use of PLV and EnvCorr is adopted in this work.

The EnvCorr is computed from the same preprocessed signals used for the PLV analysis. After the burst envelopes are extracted as the magnitudes of the analytic signals, their Pearson correlation coefficient is evaluated according to Eq. (24).

#### 4.1.3. Regime identification criteria

To improve reproducibility, empirical thresholds are introduced in the present study for the joint classification of the burst synchronization regimes. Specifically, IPB is identified when PLV $\geq 0.90$ and EnvCorr $\geq 0.60$, indicating both a stable phase relation and strongly correlated burst envelopes. PSB is identified when PLV $\geq 0.80$ and EnvCorr $\leq 0.20$, indicating that the phase relation remains relatively stable, whereas the burst envelopes are weakly correlated, shifted, or alternating. DB is identified when PLV $\leq 0.60$ and EnvCorr $\leq 0.30$, indicating weak phase locking together with poor burst-envelope coherence.

It should be noted that an intermediate region may occur when $0.60 < \mathrm{PLV} < 0.80$, or when the two indicators do not simultaneously satisfy the above threshold conditions. In this case, the boundary between PSB and DB may become less clear if only scalar thresholds are used. Therefore, for such borderline cases, the regime identification is further assisted by the PDF of the wrapped phase difference, together with the corresponding time-series and envelope evidence. Accordingly, the final classification in this paper is determined jointly from the quantitative thresholds and waveform-based evidence, rather than from a single indicator alone.

### 4.2. LEs and bifurcation analysis

To clarify the parameter-dependent dynamical evolution associated with the burst synchronization patterns, the LEs and bifurcation diagrams are evaluated for the five-dimensional map defined by Eqs. (18) under the two representative parameter sets listed in Table 1. For each value of the coupling gain $k$, the map is iterated for $N$ steps and the first $N_0$ iterations are discarded to eliminate transients. The LEs are computed by the

Benettin-QR method applied to the full Jacobian matrix, yielding five exponents denoted as LE1–LE5. The bifurcation diagrams are constructed from the post-transient samples of the fast variables $x_{1,n}$ and $x_{2,n}$. To preserve both small-amplitude details and large excursions in the plots, an $x$-compression is adopted for visualization. In addition, to better reveal the detailed dynamical evolution in the regime-transition regions, local enlargements of selected coupling intervals are provided in Figs. 4(a)–4(c) and 4(g)–4(i). For Set A, the enlarged interval is set to $k \in (-0.15, 0.2)$, while for Set B, the enlarged interval is set to $k \in (-0.35, 0.15)$. These intervals are selected to cover the representative transition regions among different burst synchronization regimes.

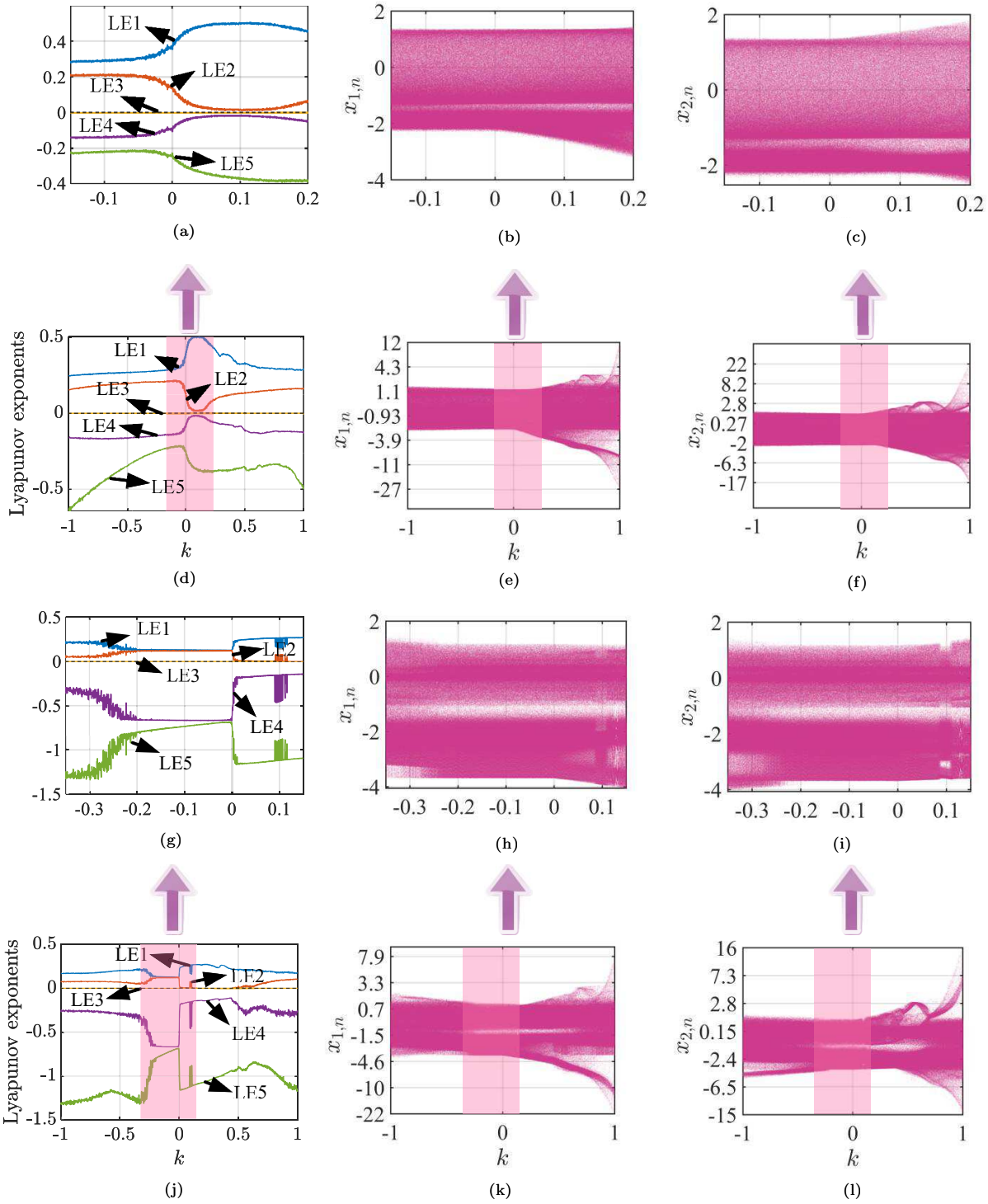



**Fig. 4.** Global and locally enlarged LEs and BDs versus the coupling gain $k$ for the memristively coupled 5D map. (a)–(c) Local enlargements of the LE spectrum and the BDs of $x_{1,n}$ and $x_{2,n}$ for Set A over $k \in (-0.15, 0.2)$. (d)–(f) Corresponding global results for Set A, where the shaded regions indicate the enlarged intervals. (g)–(i) Local enlargements of the LE spectrum and the BDs of $x_{1,n}$ and $x_{2,n}$ for Set B over $k \in (-0.35, 0.15)$. (j)–(l) Corresponding global results for Set B, where the shaded regions indicate the enlarged intervals. The displayed variables are $\tilde{x} = \mathrm{asinh}(x/s)$, where $s$ is chosen individually for each plot.

Figure 4 shows that, for both Set A and Set B, the largest Lyapunov exponent remains positive throughout the scanned interval, indicating persistent chaotic bursting. In addition, intervals with two positive Lyapunov exponents are observed, which indicates the occurrence of hyperchaotic bursting over part of the coupling range. These features are consistent with the broadband and non-periodic point distributions in the bifurcation diagrams. As $k$ increases, especially in the positive coupling region, the accessible state range expands, suggesting that the bursting dynamics become more complex and more unstable. Although the detailed transition boundaries differ between the two parameter sets, the results consistently indicate that variations in the coupling gain reorganize the coupled system within predominantly chaotic and hyperchaotic regimes. This global dynamical description provides the background for the burst synchronization regimes discussed in Subsection 4.4.

### 4.3. Equilibrium-based local interpretation

To provide a local spectral interpretation of the above parameter-dependent dynamical evolution, the equilibrium properties of the five-dimensional map are further examined. An equilibrium point is defined by the fixed-point condition in Eqs. (25) and (26), from which the equilibrium relations in Eqs. (27)–(31) are obtained. These expressions show that the equilibrium values are determined by the intrinsic fast–slow balance of the coupled system, while their existence is independent of the coupling gain $k$. Local stability is then determined by the Jacobian matrix evaluated at the equilibrium point, as given in Eq. (31).

$$\boldsymbol{X}^* = (x_1^*, y_1^*, x_2^*, y_2^*, w^*)^{\mathrm{T}}, \tag{25}$$

$$\boldsymbol{X}^* = \boldsymbol{F}(\boldsymbol{X}^*), \tag{26}$$

$$\begin{cases} x_1^* = f(x_1^*, y_1^*) + kG(w^*)(x_2^* - x_1^*), \\ y_1^* = y_1^* - \mu(x_1^* - \sigma), \\ x_2^* = f(x_2^*, y_2^*) + kG(w^*)(x_1^* - x_2^*), \\ y_2^* = y_2^* - \mu(x_2^* - \sigma), \\ w^* = (1 - \gamma h)w^* + \eta h(x_1^* - x_2^*), \end{cases} \tag{27}$$

$$x_1^* = \sigma, \quad x_2^* = \sigma, \tag{28}$$

$$w^* = 0, \tag{29}$$

$$(x_1^*, y_1^*, x_2^*, y_2^*, w^*) = (\sigma, y_1^*, \sigma, y_2^*, 0), \tag{30}$$

$$\boldsymbol{J} = \left.\frac{\partial \boldsymbol{F}}{\partial \boldsymbol{X}}\right|_{\boldsymbol{X}=\boldsymbol{X}^*}. \tag{31}$$

Figure 5 shows that, for both Set A and Set B, the maximum eigenvalue modulus remains larger than unity throughout the scanned interval, indicating that the equilibrium stays linearly unstable for all considered values of $k$. Moreover, as $k$ becomes positive, the dominant eigenvalue modulus tends to increase, implying stronger local instability. The eigenvalue distributions in the complex plane further show that multiple eigenvalues may simultaneously lie outside the unit circle, which is consistent with the emergence of hyperchaotic intervals in the Lyapunov spectra. It should be emphasized that an eigenvalue modulus larger than one only indicates the local instability of the equilibrium point and does not directly determine the existence or the detailed structure of the global chaotic or hyperchaotic attractors. Therefore, the equilibrium analysis does not serve as a complete mechanism proof but only provides a local spectral reference for understanding why the fixed point remains unstable and why positive coupling tends to enhance local instability.

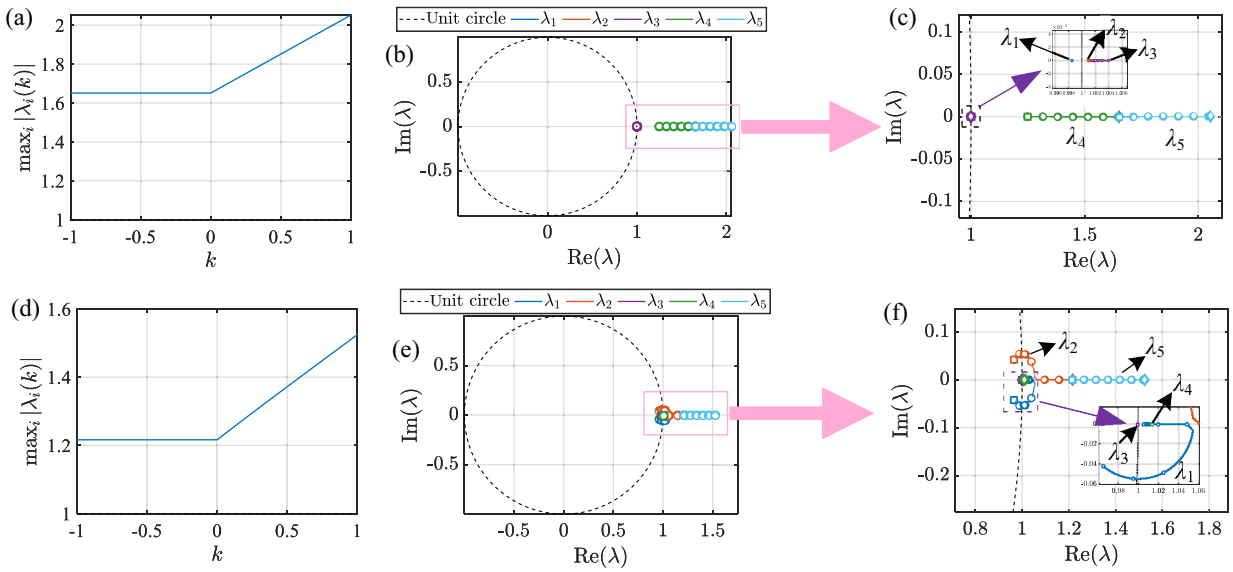



**Fig. 5.** Eigenvalue spectra of the Jacobian matrix evaluated at the equilibrium point of the five-dimensional memristive-coupled map as the coupling gain $k$ varies. Panels (a)–(c) correspond to Set A, and panels (d)–(f) correspond to Set B. (a), (d) Maximum modulus of the eigenvalues as a function of $k$. (b), (e) Distributions of the five eigenvalues in the complex plane, with the unit circle indicated by the dashed line. (c), (f) Enlarged views of the highlighted regions in panels (b) and (e), showing the detailed arrangement of unstable real and complex eigenvalues.

### 4.4. Burst synchronization regimes induced by the coupling gain

Based on the quantitative criteria introduced in Subsection 4.1.3, the burst synchronization regimes of the memristively coupled dual-Rulkov system are examined as the coupling gain $k$ varies. Figure 6 presents the corresponding PLV and EnvCorr curves for the two representative parameter sets.

For Set A, Fig. 6(a) shows that an IPB regime is sustained over a broad range of negative coupling gain. A representative case is presented in Fig. 7, where the wrapped phase-difference PDF is sharply concentrated around zero and the phase-difference trajectory fluctuates within a narrow range. The time series and phase diagram further confirm that the two neurons exhibit coherent rectangular bursting with highly correlated slow envelopes, which is consistent with the quantitative IPB criteria in Subsection 4.1.3.

As $k$ approaches zero from the negative side, the synchronization between the two neurons deteriorates and a DB regime emerges. The representative result shown in Fig. 8 indicates that the burst timing becomes irregular, the phase difference exhibits evident wandering, and its PDF becomes markedly broadened. Correspondingly, the PLV is reduced and the EnvCorr remains weak, which satisfies the low-PLV/low-EnvCorr condition of the DB regime in Subsection 4.1.3.

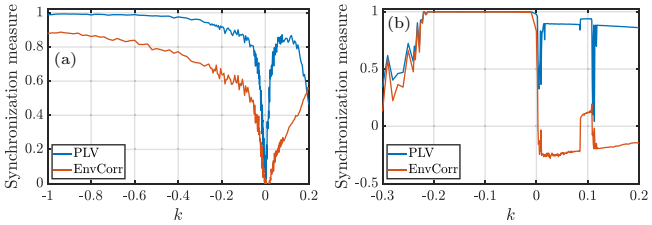



**Fig. 6.** PLV and EnvCorr versus the coupling gain $k$ for (a) Set A and (b) Set B.

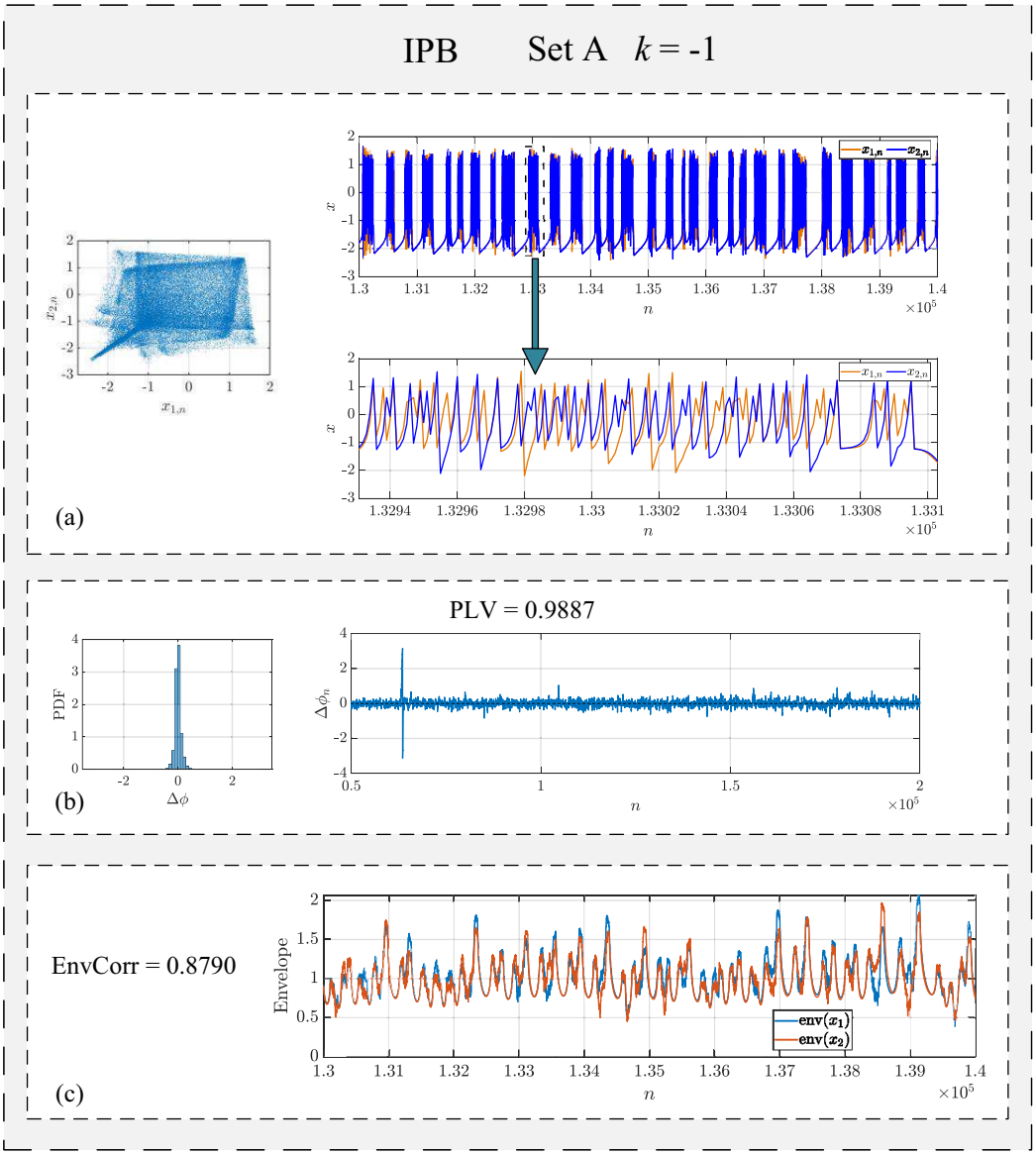



**Fig. 7.** Full evidence chain for Set A at $k = -1$. (a) Phase portrait in the plane and the corresponding time series with a zoomed-in window. (b) PDF of the wrapped phase difference $\Delta\phi$ and its temporal evolution. (c) Burst envelopes and EnvCorr evolution.

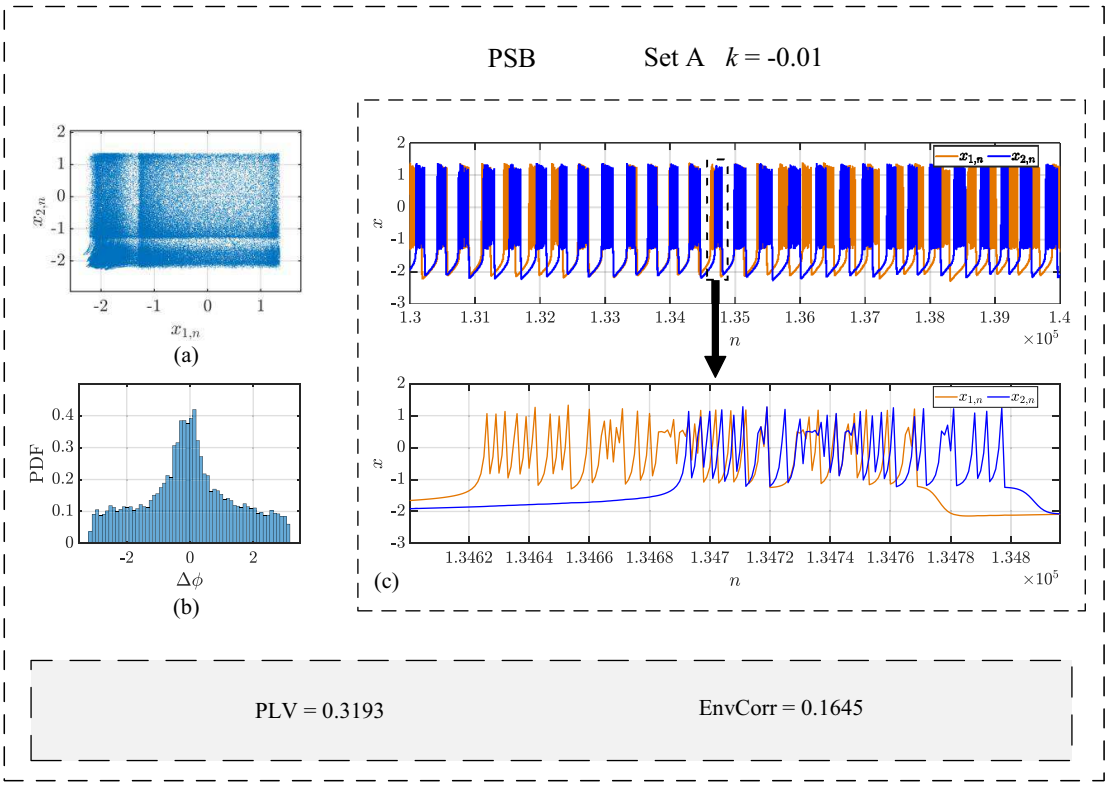



**Fig. 8.** Set A at $k = -0.01$. (a) Phase portrait in the $x_1$–$x_2$ plane. (b) PDF of $\Delta\phi$. (c) Time series with a zoomed-in window; PLV and EnvCorr values are indicated.

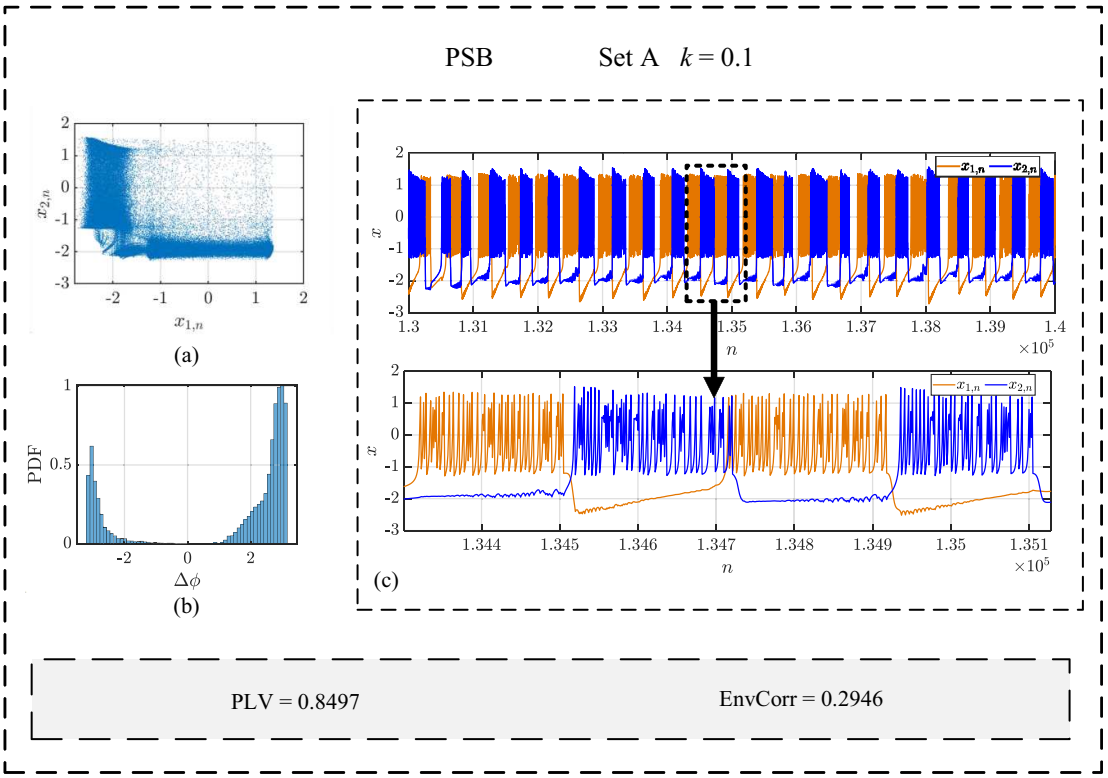



**Fig. 9.** Set A at $k = 0.1$. (a) Phase portrait in the $x_1$–$x_2$ plane. (b) PDF of $\Delta\phi$. (c) Time series with a zoomed-in window; PLV and EnvCorr values are indicated.

For small positive coupling gain, the dynamics enters a PSB regime. As shown in Fig. 9, the phase difference is no longer concentrated near zero but remains localized around a nonzero lag, so that the PLV stays relatively high. In contrast, the slow envelopes are only weakly correlated, indicating that the two neurons no longer burst in a coherent in-phase manner. This feature is consistent with the PSB criterion of relatively high PLV together with weak envelope correlation, and is further supported by the nonzero-lag phase-locking evidence in Fig. 9.

For Set B, a different regime organization is observed in Fig. 6(b). Under weak negative coupling, the system remains in a DB regime, as illustrated in Fig. 10. In this case, burst events are poorly aligned, the phase relation is not stably maintained, and the combined PLV–EnvCorr behavior is consistent with the DB criterion in Subsection 4.1.3.

When the negative coupling is moderately strengthened, the system evolves into an IPB regime. Figure 11 shows that the phase difference becomes tightly concentrated around zero, while the two triangular bursting signals exhibit strongly correlated envelope evolution. The corresponding phase portrait and time series indicate that the two neurons evolve on a highly coherent attractor, which is consistent with the quantitative IPB criteria in Subsection 4.1.3.

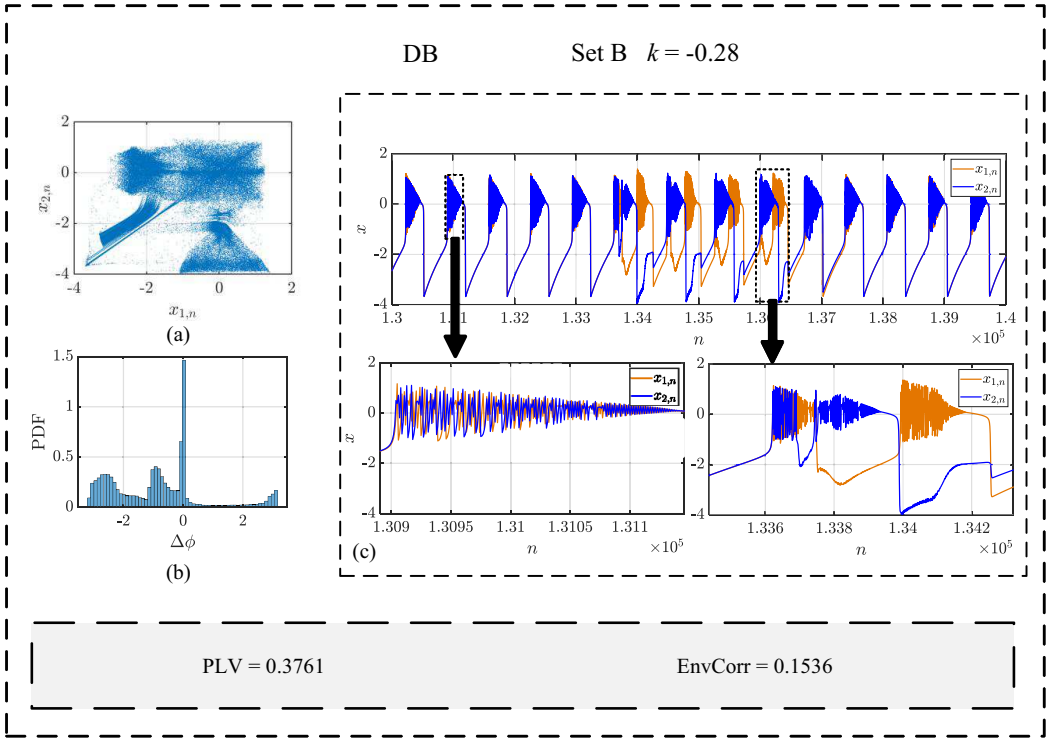



**Fig. 10.** Set B at $k = -0.28$. (a) Phase diagram. (b) PDF of $\Delta\phi$. (c) Time series with zoomed-in windows; PLV and EnvCorr are indicated.

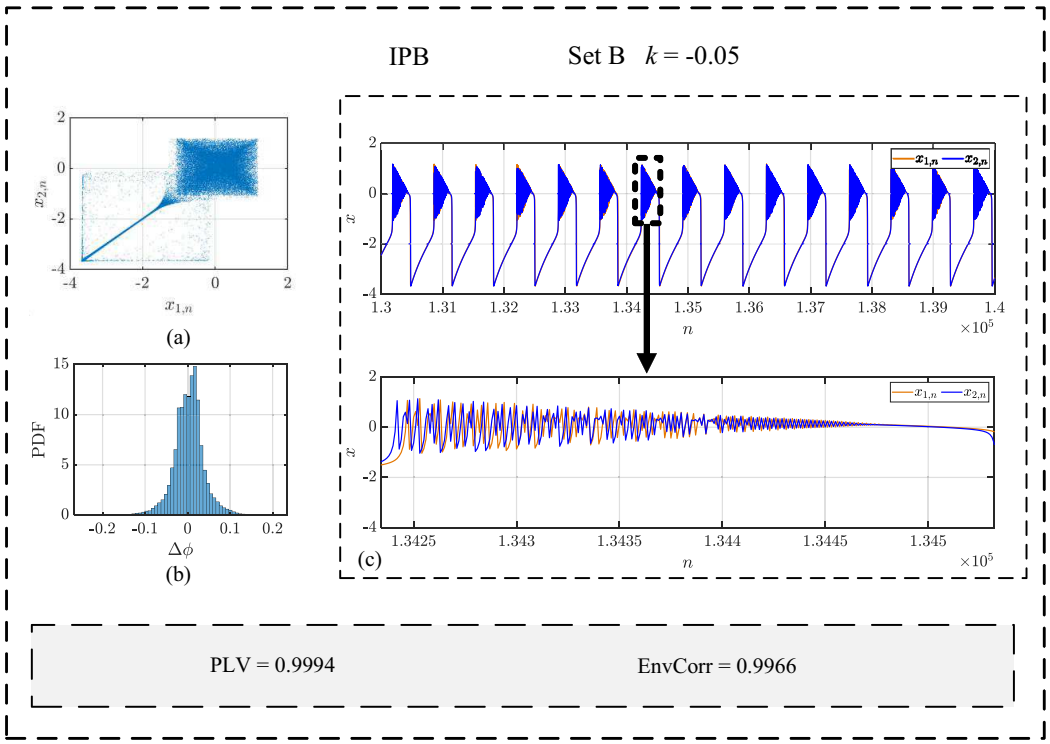



**Fig. 11.** Set B at $k = -0.05$. (a) Phase diagram. (b) PDF of $\Delta\phi$. (c) Time series with a zoomed-in window; PLV and EnvCorr are indicated.

When $k$ becomes positive, the system transitions from IPB to PSB. As shown in Fig. 12, the phase relation remains relatively stable at a nonzero lag, whereas the burst envelopes become weakly correlated or even anticorrelated. This PLV–EnvCorr combination is consistent with the PSB criterion in Subsection 4.1.3 and indicates that positive coupling favors PSB rather than coherent IPB.

Overall, Figs. 6–12 show that the coupling gain does not simply strengthen or weaken burst synchronization monotonically. Instead, it reorganizes the coupled bursting dynamics among IPB, PSB, and DB. More importantly, the joint use of PLV and EnvCorr, together with the quantitative criteria in Subsection 4.1.3 and waveform-based evidence, is essential for distinguishing these regimes. In particular, PLV alone cannot separate in-phase bursting from phase-shifted bursting, because both may exhibit a stable phase relation and hence a large PLV. EnvCorr complements this limitation by directly characterizing whether the slow envelopes evolve coherently, are weakly correlated, or evolve in an alternating manner.

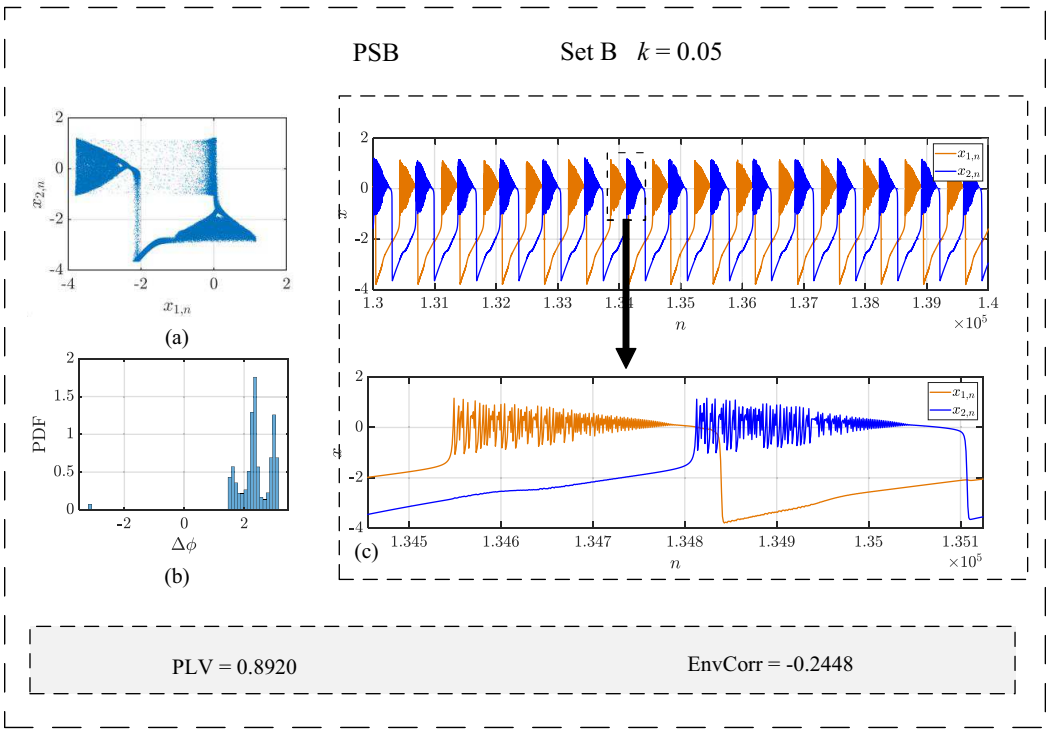



**Fig. 12.** Set B at $k = 0.05$. (a) Phase diagram. (b) PDF of $\Delta\phi$. (c) Time series with a zoomed-in window; PLV and EnvCorr are indicated.

## 5. Hardware implementation and experimental verification

### 5.1. DSP platform and hardware architecture overview

The TMS320F28335 DSP serves as the core computational platform for the real-time iteration of the five-dimensional memristive-coupled discrete neuron map. The development environment CCS 6.0 is used for programming and debugging, and the XDS100V3 emulator facilitates code downloading to the DSP board. This DSP platform offers high-precision and parallel computation capabilities, making it suitable for real-time simulation of complex dynamical systems such as the discrete neuron model.

The overall hardware architecture is illustrated in Fig. 13. The host PC is responsible for parameter setting and code downloading, which are transmitted to the DSP board via the XDS100V3 emulator. The DSP executes the real-time iterations of the five-dimensional map, which are then converted from digital signals to analog outputs by the DAC8552. These analog outputs are sent to the oscilloscope for observation in XT mode and XY mode.

For hardware implementation, the DSP directly executes the discrete iterative map defined by Eq. (18) rather than using an additional numerical integration algorithm. At each sampling cycle, the synaptic voltage difference, memductance, and coupling current are first calculated from the current state variables, and then the neuron variables together with the memristive state are updated to the next iteration. After appropriate scaling, the selected variables are output through the DAC8552 for real-time observation. In XT mode, the time-domain bursting waveforms are displayed, whereas in XY mode, the phase-plane trajectories are obtained from two simultaneously output variables.

### 5.2. DSP experimental results and qualitative validation

The DSP-based implementation reproduces representative burst synchronization behaviors under the considered parameter sets. The corresponding experimental waveforms and phase-plane trajectories are shown in Fig. 14. In XT mode, clear bursting patterns can be observed, while XY mode dis-

plays the associated attractor structures in the phase plane. These results indicate that the proposed memristively coupled dual-Rulkov system can be realized in real time on the DSP platform.

In addition to the IPB case, the PSB case is also implemented on the DSP platform. Therefore, the two cores

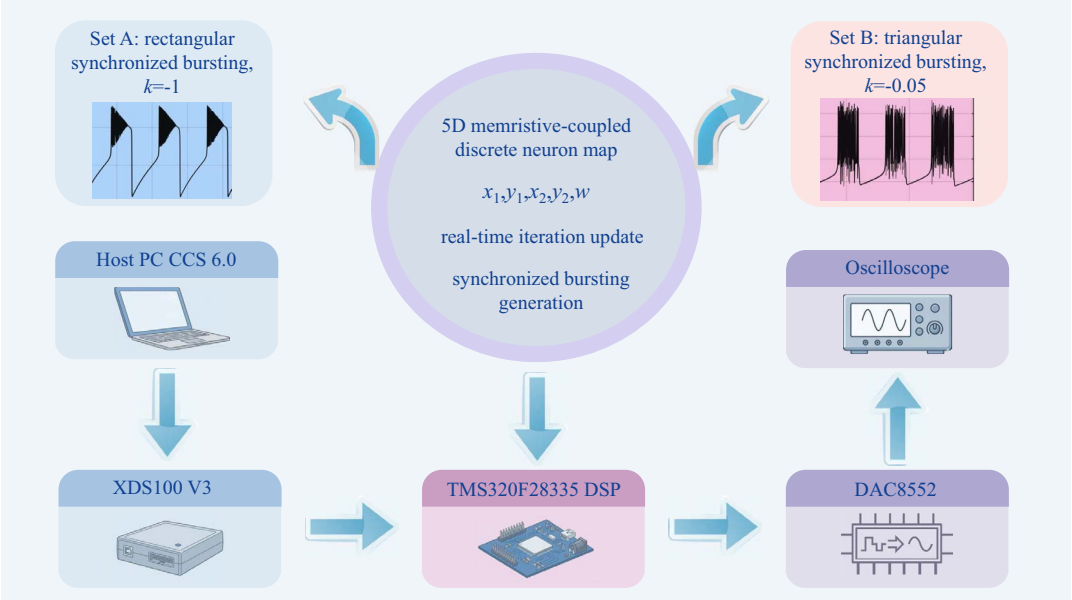



**Fig. 13.** Hardware implementation architecture of the DSP-based discrete neuron model.

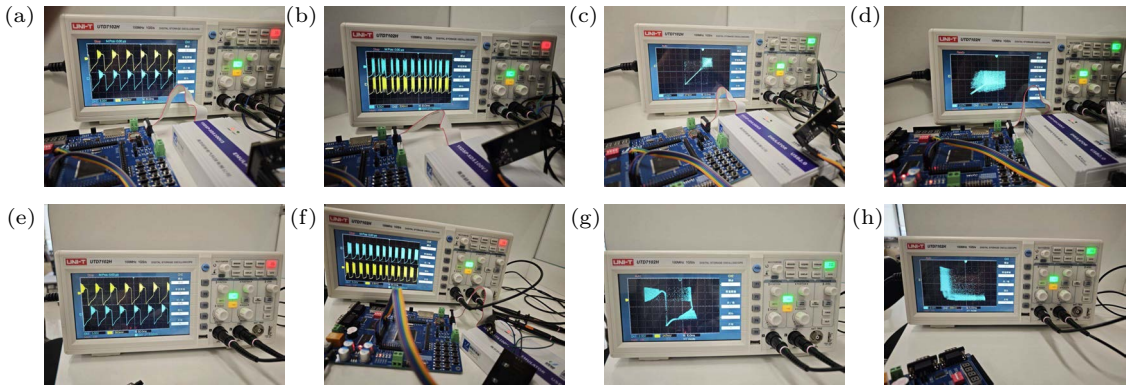



**Fig. 14.** DSP experimental results of representative IPB and PSB cases. (a), (b) XT-mode waveforms and (c), (d) corresponding XY-mode attractors of the IPB case, where (a), (c) correspond to triangular bursting and (b), (d) correspond to rectangular bursting. (e), (f) XT-mode waveforms and (g), (h) corresponding XY-mode attractors of the PSB case, where (e), (g) correspond to triangular bursting and (f), (h) correspond to rectangular bursting.

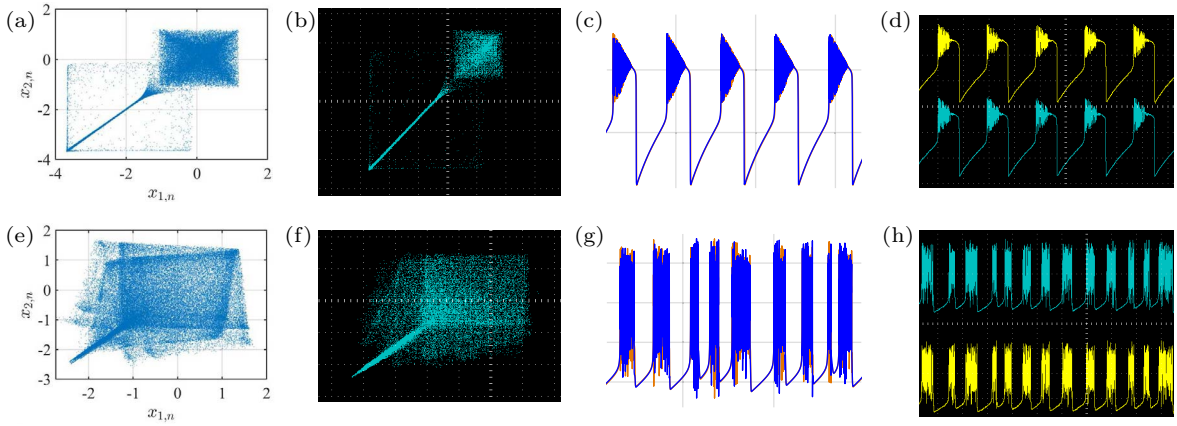



**Fig. 15.** Qualitative comparison between MATLAB simulations and DSP experimental results for representative IPB cases. (a), (b) triangular-bursting attractors from MATLAB and DSP, respectively; (c), (d) triangular-bursting waveforms from MATLAB and DSP, respectively. (e), (f) rectangular-bursting attractors from MATLAB and DSP, respectively; (g), (h) rectangular-bursting waveforms from MATLAB and DSP, respectively.

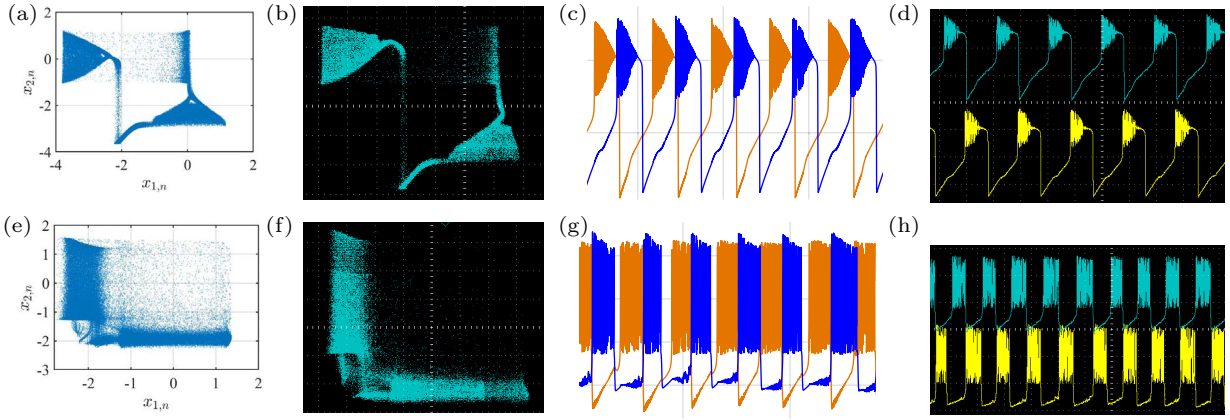



**Fig. 16.** Qualitative comparison between MATLAB simulations and DSP experimental results for representative PSB cases. (a), (b) triangular-bursting attractors from MATLAB and DSP, respectively; (c), (d) triangular-bursting waveforms from MATLAB and DSP, respectively. (e), (f) rectangular-bursting attractors from MATLAB and DSP, respectively; (g), (h) rectangular-bursting waveforms from MATLAB and DSP, respectively.

synchronization phenomena discussed in this work are both supported by representative hardware observations. The XT-mode waveforms and XY-mode attractor structures of these cases show that the DSP platform can qualitatively reproduce both in-phase bursting and phase-shifted bursting patterns.

To further examine the consistency between the hardware implementation and the numerical simulations, qualitative comparisons between the DSP experiments and MATLAB results are provided in Figs. 15 and 16. For both IPB and PSB cases, the phase-plane structures and time-domain bursting patterns obtained from the DSP experiments agree well with those produced by MATLAB simulations. The main topological features and bursting rhythms are preserved, thereby supporting the physical feasibility and real-time implementability of the proposed model.

It should be emphasized that the purpose of the present DSP experiments is to verify the qualitative consistency of the topological patterns and bursting rhythms, rather than to provide a strict quantitative validation of all theoretical indicators. Therefore, the hardware results in this work should be understood as qualitative evidence of physical realizability and pattern consistency, rather than as a complete quantitative verification.

## 6. Conclusion

In this paper, the chaotic bursting dynamics and burst synchronization behaviors of a discrete dual-Rulkov neural system coupled by a memristive synapse have been investigated. It has been shown that the constructed discrete memristive synapse model exhibits the typical PHL fingerprint together with evident local activity, thereby providing an artificial synaptic coupling mechanism with memory and nonlinear characteristics. Based on this synapse model, a five-dimensional memristively coupled discrete neural system has been established. Under the modulation of the coupling gain, rich dynamical behaviors, including chaotic and hyperchaotic bursting, have been observed. By combining Lyapunov exponent spectra, bifurcation analysis, and equilibrium stability analysis, the parameter-dependent dynamical evolution of the system has been characterized, and the corresponding equilibrium analysis has provided a local spectral interpretation of the persistent instability.

Furthermore, to characterize irregular spiking activities in chaotic bursting, a joint analysis framework based on PLV and EnvCorr has been introduced. Using this framework, three burst synchronization regimes, namely IPB, PSB, and DB, have been effectively distinguished. The results show that the coupling gain does not simply strengthen or weaken synchronization monotonically, but instead reorganizes the coupled bursting dynamics among different burst synchronization regimes. Finally, DSP-based real-time implementation has been carried out, and good qualitative agreement between the experimental results and numerical simulations has supported the physical feasibility of the proposed model. Overall, this work provides a useful framework for analyzing chaotic bursting and burst synchronization in memristively coupled discrete neural systems, and also offers a basis for the digital realization of related neuromorphic dynamical models. These results may provide useful insights for the study of burst-based information processing in neuromorphic computing systems. In addition, the proposed discrete memristive-coupled framework may serve as a potential reference for the design and analysis of artificial synaptic networks with complex dynamical behaviors.

## Acknowledgments

Project supported by the National Natural Science Foundation of China (Grant Nos. 62541206, 62502250, and 62571079), the Liaoning Provincial Science and Technology Plan Joint Project (Grant No. 2024-MSLH-033), the Liaoning Provincial Department of Education Basic Scientific Research Projects for Higher Education Institutions (Grant

Nos. LJ142510152002 and LJ142510152003), and the Dalian Science and Technology Talent Innovation Support Policy Implementation Plan–Young Science and Technology Star (Grant No. 2025RQ32).

## References


[1] Shi F, Cao Y H, Banerjee S, Ahmad A M and Mou J 2024 *Chaos Solit. Fractals* **189** 115723
[2] Meng K, Cao Y H, Xu X Y and Mou J 2025 *Integration VLSI J.* **105** 102490
[3] Chen K J and Li Z J 2025 *Nonlinear Dyn.* **113** 21769
[4] Cheng M Y, Cao Y H and Li P 2025 *Phys. Scr.* **100** 015268
[5] Buzsaki G and Draguhn A 2004 *Science* **304** 1926
[6] Hu J T, Bao H, Xu Q, Chen M and Bao B C 2024 *Chaos Solit. Fractals* **184** 114993
[7] Gao S, Shi F, Xu X, *et al*. 2026 *IEEE Trans. Consum. Electron.*
[8] Qi G Y and Wang Z M 2021 *Chin. Phys. B* **30** 120516
[9] Bi Y C, Mou J, Iu H H C, Zhou N R, Banerjee S and Gao S 2026 *Chin. Phys. B* **35** 010504
[10] Krahe R and Gabbiani F 2004 *Nat. Rev. Neurosci.* **5** 13
[11] Yu H T, Wang J A, Deng B, Wei X L, Wong Y K, Chan W L, Tsang K M and Yu Z Q 2011 *Chaos* **21** 013127
[12] Batista C A S, Lameu E L, Batista A M, Lopes S R, Pereira T, Zamora-López G, Kurths J and Viana R L 2012 *Phys. Rev. E* **86** 016211
[13] Yan X, Li Z J and Li C L 2024 *Chin. Phys. B* **33** 028705
[14] Shao Y, Wu F Q and Wang Q Y 2025 *Nonlinear Dyn.* **113** 33907
[15] Ma M L, Yuan Z Y and Zhao X 2026 *Nonlinear Dyn.* **114** 275
[16] An X L, Jiang L F, Xiong L, Zhang J G and Li X Y 2024 *Nonlinear Dyn.* **112** 16389
[17] An X L, Li Z F, Jiang L F, Xiong L and Zhang J G 2025 *Appl. Math. Model.* **147** 116203
[18] Peng Y X, Li M L, Li Z J, Ma M L, Wang M J and He S B 2025 *Neural Netw.* **185** 107213
[19] Peng Y X, Sun K H and He S B 2020 *Chaos Solit. Fractals* **137** 109873
[20] Gao S, Iu H H C, Erkan U, Simsek C, Mou J, Toktas A, Wu R and Tang X 2024 *IEEE Internet Things J.* **11** 30368
[21] Ren X Y, Cao Y H, Xu X Y, Liu X D, Gao S, Alsaadi F E and Mou J 2026 *Eur. Phys. J. Plus* **141** 23
[22] Gao S, Iu H H C, Erkan U, Simsek C, Toktas A, Cao Y H, Wu R, Mou J, Li Q and Wang C P 2025 *IEEE Trans. Circuits Syst. Video Technol.* **35** 7706
[23] Chua L O 1971 *IEEE Trans. Circuit Theory* **18** 507
[24] Strukov D B, Snider G S, Stewart D R and Williams R S 2008 *Nature* **453** 80
[25] Zidan M A, Strachan J P and Lu W D 2018 *Nat. Electron.* **1** 22
[26] Huang W, Xia X W, Zhu C, Steichen P, Quan W D, Mao W W, Yang J P, Chu L and Li X A 2021 *Nano-Micro Lett.* **13** 85
[27] Kuzum D, Yu S M and Wong H S P 2013 *Nanotechnology* **24** 382001
[28] Ma J 2026 *J. Lanzhou Univ. Technol.* **52** 165
[29] Lu J L, Ran H F, Xie D R, Zhou G D and Hu X F 2025 *Chin. Phys. B* **34** 018703
[30] Shi F, Wang K H, Cao Y H and Mou J 2026 *Neural Netw.* **195** 108291
[31] Guo M, Zhang X W, Guo W H, Dou G, Chen D, Wang L H and Iu H H C 2026 *IEEE Trans. Circuits Syst. I* **73** 1840
[32] Guo M, Zheng C G, Dou G and Iu H H C 2026 *IEEE Trans. Circuits Syst. I* **73** 850
[33] Song Y, He X, Xu X, Cao Y, Banerjee S, Gao S and Mou J 2025 *Chin. Phys. B* **34** 028703
[34] Li Z J, Xie W Q, Zeng J F and Zeng Y C 2023 *Chin. Phys. B* **32** 010503
[35] Wang C H, Liang J H and Deng Q L 2024 *Neural Netw.* **178** 106408
[36] Lu Y M, Wang C H, Deng Q L and Xu C 2022 *Chin. Phys. B* **31** 060502
[37] Zhang C K, Wang H B, Zhang Y Y and Ma C Y 2026 *Integration VLSI J.* **106** 102579
[38] Yan S H, Wang Y L, Jiang J W, Zhang J D, Zhang H B and Zhu F Y 2026 *Nonlinear Dyn.* **114** 68
[39] Izhikevich E M 2004 *IEEE Trans. Neural Netw.* **15** 1063
[40] Rulkov N F 2002 *Phys. Rev. E* **65** 041922
[41] Ramírez-Avila G M, Depickère S, Jánosi I M and Gallas J A C 2022 *Eur. Phys. J. Spec. Top.* **231** 319
[42] Wagemakers A and Sanjuán M A F 2013 *J. Franklin Inst.* **350** 2901
[43] Li Y X, Yue X T, Chang H, Han B X and Zhang Y 2026 *Chin. Phys. B* **35** 030504
[44] Wu F Q and Feng X S 2025 *Nonlinear Dyn.* **113** 28207
[45] Feng X S, Wu F Q and Ma J 2025 *Sci. China Tech. Sci.* **68** 2120402
[46] Wu X C, Gao S, Iu H H C, Chen J X, Zhang Y S, Cao Y H and Mou J 2026 *Sci. China Tech. Sci.*
[47] Yu F, Wang X Q, Yao R Y, Ying Z J, He Y and Zou Q 2026 *Integration VLSI J.* **109** 102688
[48] Song Y Q, Gao S and Xu X Y 2026 *Int. J. Bifurc. Chaos* **36** 2650019
[49] Yu F, Wang X Q, Guo R Y, Ying Z J, He Y and Zou Q 2025 *Chin. Phys. B* **34** 120501
[50] Yang F F, Song X L, He J and Yin H P 2026 *J. Zhejiang Univ. Sci. A* **27** 76
[51] Ding S Q, Wang X Y, Zhu P Y, Erkan U, Toktas A, Li Q, Mou J and Gao S 2026 *Eur. Phys. J. Plus* **141** 182
[52] Wang G Z, Gao S, Iu H H C, Zhou N R and Mou J 2026 *Chaos Solit. Fractals* **208** 118205
[53] Ding S Q, Shi F, Erkan U, Toktas A, Li Q, Wang C P, Gao S and Mou J 2026 *J. Supercomput.* **82** 225
[54] Li C B, Li Y X, Yu W N, Moroz I and Volos C 2025 *Nonlinear Dyn.* **113** 3857